WILEY InterScience®
DISCOVER SOMETHING GREAT

Electrochemical processes of nucleation and growth of hydroxyapatite on titanium supported by real-time electrochemical atomic force microscopy

Noam Eliaz, Moshe Eliyahu
Biomaterials and Corrosion Laboratory, Department of Solid Mechanics, Materials and Systems, Tel-Aviv University, Ramat Aviv, Tel-Aviv 69978, Israel

Received 12 December 2005; revised 26 February 2006; accepted 21 May 2006
DOI: 10.1002/jbm.a.30944

Abstract: Recently, interest in electrochemical formation of hydroxyapatite has evolved. In this work, highly crystalline hydroxyapatite is electrodeposited on pure titanium and Ti-6Al-4V alloy. *In situ* and *ex situ* imaging, coupled with potentiostatic and potentiodynamic measurements, is conducted by means of electrochemical atomic force microscopy. This allows for a study of the nucleation and growth of hydroxyapatite as well as of its near-atomic structure. Electrodeposition of hydroxyapatite is shown to result from precipitation in solution, following two stages: (1) instantaneous nucleation, two-dimensional growth; (2) progressive nucleation, three-dimensional growth. Although some nucleation occurs already at -842 mV, potentials that are more negative than -1.26 V versus SCE are required for enhanced growth. Mass transport is found to have only secondary effect on the deposition process. The conclusions of this work have implications in optimization of coatings on implants as well as in enhancement of the understanding of bone mineralization *in vivo*. © 2006 Wiley Periodicals, Inc. J Biomed Mater Res 80A: 621–634, 2007

Key words: AFM (atomic force microscopy); electrochemistry; hydroxyapatite coating; titanium; Ti-6Al-4V; crystal growth

INTRODUCTION

The market of orthopedic devices is growing rapidly. While titanium-based alloys exhibit many advantages for orthopedic implants,[1] their osseointegration is slow, typically taking 3–6 months. Apatite minerals are the major inorganic constituents of enamel, dentin, and vertebrate bone. Biological apatites deviate from the stoichiometric composition of hydroxyapatite (HAP), $Ca_{10}(PO_4)_6(OH)_2$, and contain small amounts of Mg^{2+}, Na^+, K^+, CO_3^{2-}, Cl^-, and F^-.[2] They have an hexagonal crystallographic structure (not close packed),[3] and grow as platelets with typical length, width, and thickness of 30–120, 25–120, and 1.5–9 nm, respectively.[4–7] The apatite crystals are typically planar with respect to the *a-c* plane.[5] Their *c*-axis in a cortical bone is generally parallel to the bone axis.[6] The size and shape of bone apatite crystals change with species, age, and disease state. Moreover, a single specimen contains a range of particle sizes and shapes, and different measurement techniques may yield different average values on polydisperse samples.[4] In their synthetic form, these bioactive ceramics are more osteoconductive than the titanium surface, and form direct bonds with adjacent hard tissues via dissolution and ion exchange with body fluids. Hence, apatite coatings, mostly plasma sprayed, are often applied on metals and alloys.

Recently, much interest in electrodeposition has evolved due to (1) the low temperatures involved, which enable formation of highly crystalline deposits with low solubility in body fluids and low residual stresses, (2) the ability to coat porosive, geometrically complex or non line-of-sight surfaces, (3) the ability to control the thickness, composition, and microstructure of the deposit, (4) the possible improvement of the substrate/coating bond strength, and (5) the availability and low cost of equipment.

The course of crystal growth reactions and the properties of the electrodeposits may markedly be influenced by surface preparation of the substrate, bath chemistry, oxygen level, pH, stirring, the applied potential (or current density), temperature, and cell geometry. Defects on the surface play a major role in the nucleation and growth of electrodeposits.[8] The solubility isotherms show that HAP becomes thermodynamically more stable compared to other calcium

Correspondence to: N. Eliaz; e-mail: neliaz@eng.tau.ac.il
Contract grant sponsor: Dan David Prize
Contract grant sponsor: Ella Kodesh Foundation

phosphate phases as the pH increases.[9,10] Stirring has been once reported to decrease the crystal size, indicating an increase in the number of nucleation sites.[11] This may result from either mass transport limitation or preferred nucleation on the metal surface as compared to the surface of a weakly bonded calcium phosphate. The formation of reasonably thick, highly crystalline, stoichiometric HAP usually requires heating of the bath. For example, Eliaz et al. found that temperatures higher than 70°C are required for electrodeposition of HAP on pure Ti from a bath containing 0.61 m*M* $Ca(NO_3)_2$ and 0.36 m*M* $NH_4H_2PO_4$ at pH 6.0 and $E = -1.4$ V versus saturated calomel electrode (SCE).[12]

Several studies have involved *ex situ* high resolution transmission electron microscopy (HRTEM) and/or atomic force microscopy (AFM) of calcium phosphates produced under different conditions.[13–16] Manso et al. used both AFM and HRTEM to study the structure of thin (<0.3 μm) sodium- and carbonate-containing HAP that was grown from a basic solution (pH 9.1) on Si (100) and Ti/Si (100) surfaces, either spontaneously or by +2 V activation.[13] Surface enrichment with hydroxyl ions, $(OH)^-_{ads}$, due to the application of a positive potential resulted in numerous nucleation sites and finer grains of HAP compared to the non-activated condition. Onuma et al. used AFM and phase shift interferometry to observe the surface topography of the $(10\bar{1}0)$ face of HAP single crystals synthesized from a hydrothermal solution.[16] The growth was observed to proceed through a layer-by-layer mechanism.

Yet, as per to-date, no direct, *in situ* and real-time observation of the electrochemical nucleation and growth of HAP has been reported. The electrochemical scanning probe microscope enables to combine real-time imaging of surfaces at near-atomic resolutions with electrochemical measurements. Thus, it is possible to study the effect of the substrate surface, bath chemistry, and process parameters on the kinetics and thermodynamics of deposition as well as on the microstructure of deposits. The objective of this work is to demonstrate the viability of the electrochemical atomic force microscope (EC-AFM), in conjunction with electrochemical measurements in standard macrocells, for understanding the mechanisms of nucleation and growth of HAP.

EXPERIMENTAL

A sheet made of pure Ti grade 2 and a rod made of Ti-6Al-4V grade 5 (both supplied by Scope Metal Trading and Technical Services) were used as cathodes. Electrical discharge machining was used to cut slices of rod. Prior to electrodeposition, the cathode was mechanically ground on SiC papers from P120 to P1000 grit, polished on a cloth with colloidal silica, rinsed with DI water, cleaned ultrasonically in acetone, rinsed again with DI water, and dried. Several rod samples were also electropolished in H_2SO_4 bath at room temperature and at 2 V for 2 min, and subsequently etched chemically in Kroll solution for 5 s, in order to expose the dual phase structure. The open-circuit potential of the working electrodes after these treatments was around −100 mV versus SCE. Electrodeposition was carried out in a three-electrode cell. The bath contained 0.61 m*M* $Ca(NO_3)_2$ and 0.36 m*M* $NH_4H_2PO_4$ (AR-grade, Merck) in Milli-DI^{TM} water (Millipore). The pH was adjusted to 6.0 by NaOH additions and measured by InoLab pH/Oxi Level 3 meter (WTW). These concentration ($[Ca^{2+}]/[PO_4^{3-}] = 1.67$) and pH values were chosen, to assure formation of stoichiometric HAP based on solubility isotherms for calcium phosphates.[9,10] The exposed surface area of the working electrode (cathode) was either 1 cm^2 or ∼0.205 cm^2 in the macrocell and AFM liquids cell, respectively. A Pt foil and a Pt wire were used as counter electrodes (anodes) in the standard macrocell and AFM liquids cell, respectively. A SCE and a Pt wire were used as reference and quasireference electrodes in the former and latter cell, respectively. Preliminary measurements in a macrocell ($T = 60°C$, no nitrogen purging) showed that 167 min are required for the Pt wire to reach steady state at $E = 398 \pm 10$ mV versus SCE. Therefore, all of the *in situ* experiments started only after the Pt wire was allowed to reach steady state. During deposition, both nitrogen gas (99.999% purity) purging and magnetic stirring were used in the macrocell only. The temperature was maintained at a constant temperature within a range of 60–90°C by means of an oil bath or a temperature controller (0.10 K, Lakeshore) in the macrocell and AFM cell, respectively. An EG&G/PAR 263A potentionstat/galvanostat was used for electrochemical control and measurements in the macrocell, whereas a PicoStat bi-potentionstat/galvanostat (Molecular Imaging) was used with the AFM. All potentiostatic experiments were carried out at $E = -1.4$ V versus SCE.

Potentiodynamic experiments at a scan rate of 0.5 mV s^{-1} were conducted in the macrocell both in the standard electrolyte mentioned earlier and in a supporting electrolyte, where the 0.61 m*M* $Ca(NO_3)_2$ was replaced by 1.22 m*M* $NaNO_3$. Because sodium phosphate is soluble in aqueous solutions, the subtraction of currents measured in the supporting electrolyte from currents measured in the standard electrolyte provides the net current associated with nucleation and growth of HAP. Preliminary cyclic voltammetry (CV) experiments were also carried out in a macrocell, with a standard electrolyte at 60°C. Usually, CV experiments are conducted at a scan rate within the range of 0.01–100 V s^{-1}. In our case, a series of experiments was first carried out at different scan rates from 500 to 50 mV s^{-1}, with 50 mV s^{-1} decrements. A scan rate of 100 mV s^{-1} was found the fastest to still yield overlap of voltammograms. At this scan rate, stirring had a detectable effect (in the form of a moderate increase in current density), and only once the potential was scanned to below approximately −0.8 V versus SCE. Hence, mass transport limitation may exist only at potentials more cathodic than this value.

A PicoSPM^{TM} (Molecular Imaging) EC-AFM was used both *in situ* and *ex situ*. The AFM was preferred over the scanning tunneling microscope, despite the compromise in resolution, because of the nonconducting character of HAP. Imaging was done under contact mode, using tips made of Si_3N_4 (Veeco). The small volume of the warm electrolyte (∼1 cm^3) limits the duration of *in situ* experiments and likely introduces a more significant pH change during deposition. *In situ* CV and cathodic polarization experiments were conducted at 5 mV s^{-1} while imaging the surface. This very slow scan rate allowed for correlating the acquired image with the cyclic voltammogram.

The surface morphology of deposits was imaged in a JSM-6300 scanning electron microscope (SEM, Jeol). The attached energy dispersive spectroscopy (EDS, Oxford Isis) was used to estimate the Ca/P ratio and to perform X-ray mapping of various elements. The structure of deposits was analyzed by X-ray diffraction (XRD, Scintag).

RESULTS

Electrocrystallization (i.e., the nucleation and crystal growth in electrochemical systems under the influence of an electric field) can be treated in a similar manner to that of deposition from a vapor phase. The nucleation type can be either instantaneous or progressive, and the growth mode can be one-, two-, or three-dimensional, with the resulting shape of growing crystallites being, for example, needles, discs, and either cones or hemispheres, respectively. The rate-determining step may be charge transfer, cylindrical diffusion, hemispherical diffusion, or ohmic polarization. Different combinations of nucleation type, growth mode, and rate-determining step yield different functions of current density as a function of time.[17]

The nucleation process on real crystalline substrates (i.e., those with crystal defects and/or inhomogeneities that result in preferred nucleation sites) with a fixed number, N_0, of randomly distributed, equally active sites may be described by the following first-order kinetics law[17–19]:

$$N = N_0[1 - \exp(-At)] \tag{1}$$

where N is the number of sites converted into nuclei at time t and A is a nucleation rate constant (the inverse of the mean nucleation time). When A is very high, $N \cong N_0$, all surface sites are converted immediately into nuclei, and the nucleation is said to be "instantaneous". On the other hand, when A and t are both small, $N \cong AN_0t$, the number of nuclei depends on time, and the nucleation is termed "progressive". In this case, nuclei appear arbitrarily in space and time, eventually forming a monolayer. Note that, in practice, nucleation is said to be instantaneous whenever the rate of formation of a nucleus at a given site is expected to be at least 60 times greater than the expected rate of coverage of the site by the act of growth only. On the other hand, the nucleation is called progressive when the expected coverage of a site by the act of growth is at least 20 times greater than the coverage of the same site by the act of nucleation.[20]

The most important parameters determining the mode of growth of a substance on a foreign substrate are the deposit/substrate binding energy and the crystallographic misfit between them. Considering the deposition process at nearly equilibrium conditions, that is, small supersaturation and negligible kinetic influences, a deposit may grow on a substrate by different modes.[17] First, if the binding energy between adsorbed deposit ions is lower than the binding energy between an adsorbed ion and a substrate atom, and the crystallographic misfit is negligible, growth takes place layer-by-layer according to the Frank–van der Merwe model up to the disappearance of the strong substrate-deposited substance attraction.[21] Second, if the binding energy between adsorbed deposit ions is higher than the binding energy between an adsorbed ion and a substrate atom, formation of three-dimensional islands occurs according to the Volmer–Weber model,[22] regardless of the crystallographic misfit. Third, if the binding energy between adsorbed deposit ions is lower than the binding energy between an adsorbed ion and a substrate atom, and the crystallographic misfit is significant, formation of strained two-dimensional layers is followed by growth of unstrained three-dimensional islands according to the Stranski–Krastanov model.[23]

Figure 1(a) shows the current density transients monitored during potentiostatic deposition at −1.4 V versus SCE. The shape of these transients is similar to that drawn for theoretical transients in the presence of overlap between diffusion fields around growing nuclei.[8] The transients may be divided into four periods. Initially, charging of the double layer leads to a rapid current decay. Next, the current starts to increase either due to growth of independent nuclei or due to growth of dependent nuclei and simultaneous increase in the number of nuclei. During this second period, three-dimensional diffusion toward the growing surface occurs in the absence of overlap. During the third period, an overlap between diffusion fields around growing nuclei introduces a one-dimensional diffusion limit, while growth of independent nuclei still occurs. Consequently, the nucleation rate decreases gradually until, eventually, the growth centers contact one another and the growth stops. During the last, fourth period, the overall current decreases slowly as a result of a decrease in the effective surface area of the electrode and a change from a hemispheric mass transport condition to a linear mass transport condition. Based on Figure 1(a), it may be concluded that after ~12 min at 80–85°C, the HAP deposit changes its morphology from two-dimensional to three-dimensional. This conclusion is supported by microscopic observations, as will be demonstrated later.

Scharifker and coworkers derived analytical expressions for multiple nucleation phenomena followed by diffusion-controlled growth of three-dimensional is-

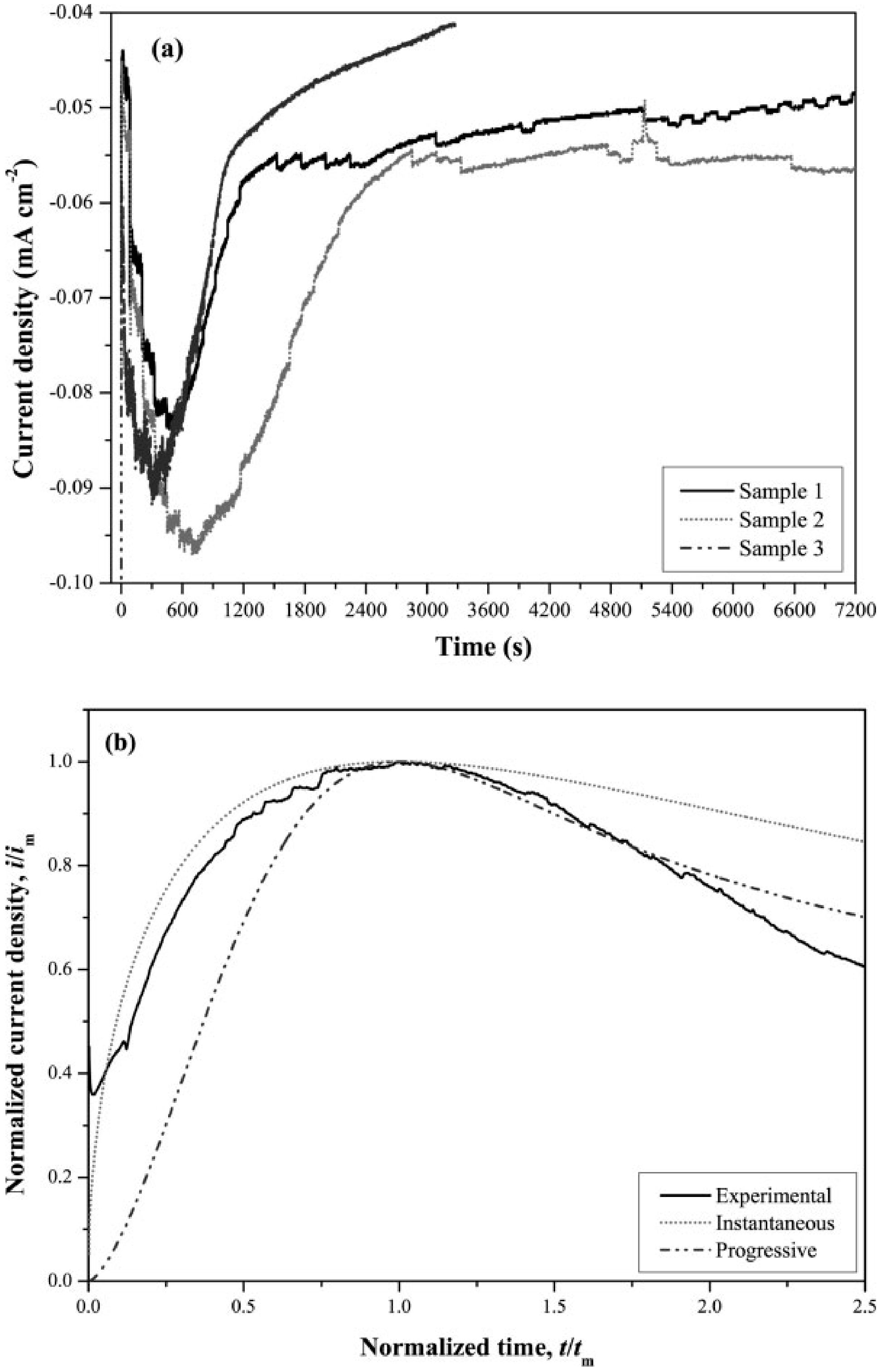

Figure 1. Current density transients during electrodeposition of HAP on pure Ti. (a) Experimental data from three potentiostatic depositions in a macrocell at $T = 80–85°C$. The transients may be divided into four time regimes where different processes prevail. (b) A normalized experimental transient is compared to the counterpart calculated curves for instantaneous and progressive nucleation models. A change is observed from instantaneous nucleation at shorter deposition periods to progressive nucleation at longer periods.

lands.[24,25] Their model defines current as the product of charge density by velocity of ions. Assuming a hemispherical growth for the nuclei and a regular diffusion process for the ions in the solution, they arrived at an expression for current density, where the overlap of adjacent nuclei was taken into account via Avrami theorem. The resulting expressions for the normalized current densities allow to distinguish between instantaneous nucleation and progressive nucleation[24,26]:

$$\frac{i^2}{i_m^2} = 1.9542\frac{t_m}{t}\left[1 - \exp\left(-1.2564\frac{t}{t_m}\right)\right]^2 \quad \text{instantaneous} \tag{2.1}$$

$$\frac{i^2}{i_m^2} = 1.2254\frac{t_m}{t}\left[1 - \exp\left(-2.3367\frac{t^2}{t_m^2}\right)\right]^2 \quad \text{progressive} \tag{2.2}$$

where i_m is the maximum current density in the current density transient and t_m is the time at this maximum point.

Figure 1(b) is a normalized representation of an experimental current density transient with $t_m = 1108$ s and $i_m = -88.3$ μA cm^{-2}. For comparison, the calculated curves for instantaneous nucleation and progressive nucleation are also drawn. It is evident that while at times shorter than t_m the experimental curve fits better the instantaneous nucleation model, at times longer than t_m it better fits the progressive nucleation model. The deviation of the experimental curve from the theoretical curves may be explained in terms of both accompanying cathodic reactions in which the charge is transferred, and precipitation from solution (see later) instead of direct nucleation on the solid electrode surface. The change from instantaneous nucleation to progressive nucleation may be attributed to porosity and nonuniform electrical fields in the ceramic HAP coating, as well as to changes in the pH and composition of the solution during the experiment. It should be noted that a similar change occurs in electrodeposition of metal on metal or metal on semiconductor, only when the applied potential is changed, and that in these cases the time scale for instantaneous nucleation is much shorter (namely, t_m is typically within the milliseconds to seconds range) than that in the experiments reported herein. These differences further support the claim that the mechanism of electrodeposition of HAP is basically different from conventional electrodeposition of metals. It can also be hypothesized that the rate of coverage of electrode surface sites by the act of HAP growth only is very slow under the studied conditions,[20] and so instantaneous nucleation can still require fairly long deposition time periods. In addition, one should recall that the model of Scharifker and Hills[24] lacks a description of the dynamic interaction between chemical species in the solution and neglects the influence of reduction/oxidation rates and of external variables such as the applied potential.[27] For example, a small decrease of 70 mV versus SCE in the cathodic overpotential has been reported to result in an increase by more than one order of magnitude in t_m for electrocrystallization of Cu on Pt.[28]

Next, the electrochemical and chemical reactions involved in the deposition of HAP are summarized. When a voltage is applied, several electrochemical reactions may occur:

$$O_2 + 2H_2O + 4e^- \rightarrow 4(OH)^-_{ads} \tag{3.1}$$

$$2H^+ + 2e^- \rightarrow H_2 \tag{3.2}$$

$$2H_2O + 2e^- \rightarrow H_2 + 2(OH)^-_{ads} \tag{3.3}$$

$$NO_3^- + H_2O + 2e^- \rightarrow NO_2^- + 2(OH)^-_{ads} \tag{3.4}$$

$$TiO_2 + 2H_2O + e^- \rightarrow Ti(OH)_3 + (OH)^-_{ads} \tag{3.5}$$

$$H_2PO_4^- + H_2O + 2e^- \rightarrow H_2PO_3^- + 2(OH)^-_{ads} \tag{3.6}$$

$$H_2PO_4^- + e^- \rightarrow HPO_4^{2-} + \frac{1}{2}H_2 \tag{3.7}$$

$$H_2PO_4^- + 2e^- \rightarrow PO_4^{3-} + H_2 \tag{3.8}$$

$$HPO_4^{2-} + (OH)^-_{ads} \rightarrow PO_4^{3-} + H_2O \quad \text{or} \quad HPO_4^{2-} + e^- \rightarrow PO_4^{3-} + \frac{1}{2}H_2 \tag{3.9}$$

Reactions (3.1) through (3.6) all lead to a local increase in pH within the diffusion layer. The increase in the concentration of the hydroxyl ions results in an increase in the concentration of phosphate ions that are required for the deposition of HAP, according to reaction (3.9). Chemical, acid–base reactions may also provide the necessary phosphate ions even in the absence of applied voltage.

The equilibrium reactions for decomposition of phosphoric acid at 25°C are defined as follows[29,30]:

$$H_3PO_4 \rightleftharpoons H_2PO_4^- + H^+ \tag{3.10}$$

$$H_2PO_4^- \rightleftharpoons HPO_4^{2-} + H^+ \tag{3.11}$$

$$HPO_4^{2-} \rightleftharpoons PO_4^{3-} + H^+ \tag{3.12}$$

Reaction (3.11) is an important biological buffer system that operates in the internal fluid of all cells. The acid dissociation equilibrium constants for reactions (3.10–3.12) at 37°C are $K_{a1} = 5.88 \times 10^{-3}$, $K_{a2} = 6.85 \times 10^{-8}$, and $K_{a3} = 4.35 \times 10^{-13}$, respectively.[30] Hence, for equal concentrations of hydrogen phosphate ions and phosphate ions in reaction (3.12), p$K_{a3} = 12.36$. This means that the local pH must increase significantly from the initial value of 6.0, before chemical reactions start playing a significant role in the supply of phosphate ions for deposition of HAP. In practice, this difference of 6.36 pH units means that the concentration of phosphate ions formed in a simple acid–base reaction is approximately six orders of magnitude smaller than the concentration of the hydrogen phosphate ions in solution and may thus be neglected herein. The actual pH in the vicinity of the cathode was not monitored during deposition in the present work. Nevertheless, a rough estimation was made based on a third-order polynomial fitting of data from Zhang et al.,[31] who used a pH microsensor to measure *in situ* the pH as a function of current density. This fitting yielded the relation:

$$\mathrm{pH} = 0.0525\, i^3 - 0.5455\, i^2 + 2.1558\, i + \mathrm{pH}_0 \qquad (4)$$

where i is the current density (absolute value in units of mA cm^{-2}) and pH_0 is the initial pH of the bulk solution (i.e., before application of current). Substituting a value of $i = 424\ \mu\mathrm{A\ cm}^{-2}$, which corresponds to $E = -1.4$ V versus SCE in one of the potentiodynamic polarization measurements in the present work, into Eq. (4)—an estimated value of pH 6.8 is found. This value is much lower than $\mathrm{p}K_{\mathrm{a}3}$. Moreover, for an electrolyte that initially contains 0.36 mM $\mathrm{H_2PO_4^-}$ at pH 6.0, it can be shown that $\log[\mathrm{PO_4^{3-}}] = 2\ \mathrm{pH} - 22.97$, meaning that pH $\sim$ 9.8 is required to fully consume the 0.61 mM $\mathrm{Ca^{2+}}$ in solution while forming HAP. It is thus concluded that the local pH is not actually high enough to allow chemical reactions, being significant in production of phosphate ions. However, this raise in pH makes the formation of HAP more favorable thermodynamically compared to other calcium phosphate phases.[9] It should be noted that Eq. (4) is only a rough approximation of the real conditions in the present study, because it is based on experimental data which was constructed under galvanostatic conditions at an initial pH 4.5 and cell volume different from that in the present work. Although the equation was adjusted for an initial pH 6.0 during its construction, it cannot be excluded that the derivative of pH on time is slightly different in both studies.

Even when significant concentrations of phosphate ions are produced by reduction of hydrogen phosphate ions and dihydrogen phosphate ions as in reactions (3.8), (3.9), and (3.12), one should consider the fast kinetics of the phosphate ions recombination with hydrogen ions [the reversal of reaction (3.12)]. This implies that the concentration of calcium ions in solution must be high compared to the concentration of hydrogen ions, thus statistically allowing physical precipitation of HAP in solution in accordance with the reaction:

$$10\mathrm{Ca^{2+}} + 6\mathrm{PO_4^{3-}} + 2(\mathrm{OH})^- \rightleftharpoons \mathrm{HAP} \qquad (3.13)$$

The experimental conditions in the present work satisfy this requirement, with the concentrations of calcium and hydrogen cations being 0.61 mM and 1.0 μM, respectively.[32]

In order to determine which of the chemical and electrochemical reactions (3.1) through (3.13) are mostly reflected by current density measurements, calculations of the limiting current density i_L were carried out following Fick's first law in the absence of stirring:

$$i_\mathrm{L} = \frac{zFDc}{\delta} \qquad (5.1)$$

where z is either the number of electrons transferred in the reaction or the valence of the species, F the Faraday's constant (96,485.3 C mol^{-1}), D the diffusion coefficient of the relevant species, c the concentration of the reactant in the bulk solution, and δ is the thickness of the diffusion layer. By definition, the limiting current density is the maximal current density that can be reached in an electrode reaction for a given concentration of reactant in the presence of excess supporting electrolyte. It results from inability of the reactant concentration on the surface of the electrode to change anymore as to provide the concentration gradient that is necessary for the diffusion flux. Table I summarizes the values substituted into Eq. (5.1) for each possible cathodic reaction. In most cases, $D \sim 10^{-5}\ \mathrm{cm^2\ s^{-1}}$, as typical for diffusion of gases and ions in aqueous solutions.[33] The thickness of the diffusion layer in the absence of stirring (i.e., as in the AFM liquids cell) can be estimated based on the relation:

$$\delta = \sqrt{\pi D t} \qquad (5.2)$$

where $t = 100$ s is applied as the maximal time at which convection is still not involved. Thus, one obtains $\delta \sim 5.6 \times 10^{-2}$ cm. In contrast, when the electrolyte is stirred (e.g., as in the macrocell), the thickness of the diffusion layer decreases as a function of the stirring velocity, and then $\delta \sim (1\text{–}3) \times 10^{-2}$ cm is more likely. In Table I, the value $\delta = 2 \times 10^{-2}$ cm within this range is used. Another assumption in our calculations is that the electrolyte is aerated, that is, in contact with air. In several cases, instead of a typical value of diffusion coefficient, our references listed the typical value of the ion mobility, u, in an aqueous solution at 25°C. In these cases, the value of the diffusion coefficient was calculated based on the Einstein's equation:

$$D = \frac{uRT}{zF} \qquad (5.3)$$

where R is the ideal gas constant (8.314 J $\mathrm{mol^{-1}\ K^{-1}}$) and T is the absolute temperature.

Several conclusions may be drawn based on Table I. First, only reaction (3.3), that is, electrolysis of water,

TABLE I
Limiting Current Density Values for Different Cathodic Reactions Obtained From Eq. (5.1) by Substituting the Parameter Values

Reaction	Ion/Molecule	Reacting Species	z	D ($cm^2\ s^{-1}$)	c ($mol\ cm^{-3}$)	i_L ($\mu A\ cm^{-2}$)
3.1	O_2	O_2	4	1.9×10^{-5} [a]	2.2×10^{-7} [b]	81
3.2	H_3O^+ (H^+)	H^+	1	9.3×10^{-5} [c]	1.0×10^{-9} [d]	0.45
3.3	H_2O	H^+	1	2.4×10^{-5} [e]	5.56×10^{-2} [f]	6.4×10^6
3.4	NO_3^-	N^{5+}	2	1.9×10^{-5} [c]	1.22×10^{-6} [g]	224
3.5	TiO_2	Ti^{4+}	1	N/A	N/A	N/A
3.6	$H_2PO_4^-$	P^{5+}	2	$\sim 8.0 \times 10^{-6}$ [h]	3.6×10^{-7} [i]	28
3.7	$H_2PO_4^-$	P^{5+}	1	$\sim 8.0 \times 10^{-6}$ [h]	3.6×10^{-7} [i]	14
3.8	$H_2PO_4^-$	H^+	2	$\sim 8.0 \times 10^{-6}$ [h]	7.2×10^{-7} [i]	56
3.9	$HPO_4{}^{2-}$	H^+	1	$\sim 8.0 \times 10^{-6}$ [h]	2.2×10^{-8} [j]	0.85
3.13	Ca^{2+}	N/A	N/A	$\sim 1.0 \times 10^{-5}$	6.1×10^{-7} [k]	N/A

[a] According to Ref. 17.

[b] The concentration of oxygen dissolved in water at 35°C.

[c] Based on ion mobility data.

[d] The concentration of hydrogen cations at pH 6.0. The formation of hydrogen cations by buffer dissociation is neglected based on reaction (3.11) and the corresponding equation defining K_{a2}.

[e] The self diffusion coefficient for water at 25°C.

[f] The concentration of pure water is 55.6*M* (the ratio between density and molecular weight of water). This concentration does not change as a result of reactions in dilute aqueous solutions.

[g] The concentration of the nitrate ions is twice the concentration of $Ca(NO_3)_2 \cdot 4H_2O$ in solution.

[h] According to Ref. 17 for H_3PO_4.

[i] The concentration of the phosphate ions is equal to the concentration of $(NH_4)H_2PO_4$ in solution. The dissociation of the latter may be neglected according to reaction (3.11).

[j] The concentration of the hydrogen cations which is equal to the concentration of HPO_4^{2-} based on the equation defining K_{a2} at pH 6.0.

[k] The concentration of calcium ions is equal to the concentration of $Ca(NO_3)_2$ in solution.

can produce high current densities that prevent the detection of a limiting current density in the cyclic voltammograms (as will be demonstrated later). Second, reduction of nitrate ions [reaction (3.4)] is not negligible under the potential applied in this work. Third, reaction (3.8) is more dominant than reaction (3.9) in the supply of phosphate ions (i_L equals 56 $\mu A\ cm^{-2}$ and 0.85 $\mu A\ cm^{-2}$, respectively). The reduction of titanium oxide does not involve any diffusion limitations and, therefore, should not affect the limiting current density.

In electrochemistry, the nature of electrode reactions can often be determined based on mathematical expression of the peak current in CV. Possible processes include (1) a reversible, Nernstian process, for which the peak current in the absence of stirring is proportional to the square root of the potential scan rate; (2) an irreversible process, for which the peak current is also proportional to the square root of the scan rate; (3) a surface reaction, for which the peak current is proportional to the scan rate but is not affected by stirring; and (4) a quasistable process, for which only secondary parameters may make the peak current dependent on the scan rate.[34] In this work, stirring was found to affect the current density at potentials negative than −0.8 V versus SCE. Hence, process (3) may be excluded. Figure 2 shows three cyclic voltammograms that were constructed in a macrocell at different scan rates and were each normalized by the square root of its own scan rate. While the normalized anodic current increases as the scan rate is increased, the normalized cathodic current decreases. It should be noted that before normalization, the same voltammograms overlapped on the cathodic side. Because the normalized voltammograms do not overlap, it may be concluded that mass transport, either reversible (1) or irreversible (2), may have only a secondary role in deposition of HAP. Hence, charge transfer most likely controls the process kinetically.

In several papers, deposition of apatite bioceramics from electrolytes has been assumed to follow one or more of the following reactions: (1) electrochemical reactions, (2) acid–base reactions, and (3) physical precipitation from solution.[31,35–42] Here we suggest the model shown in Figure 3 for the formation of HAP by electrodeposition. According to this model, a sufficient cathodic potential allows for various interplays among electrochemical reactions, chemical reactions, and local pH increase. The three possible routes all result in precipitation of HAP in solution.

Before presenting the *in situ* EC-AFM observations, let us analyze the structure of the HAP deposits as determined *ex situ* by various characterization techniques. Figure 4 demonstrates the surface morphology of electrodeposited HAP as revealed by SEM. The deposit is constructed from platelets with a typical width of several microns and a submicron thickness. A complementary, independent environmental SEM (ESEM) study shows that the deposit is composed of two layers: (1) A uniform, 500-nm thick dense layer adjacent to the substrate; and (2) a thicker layer composed

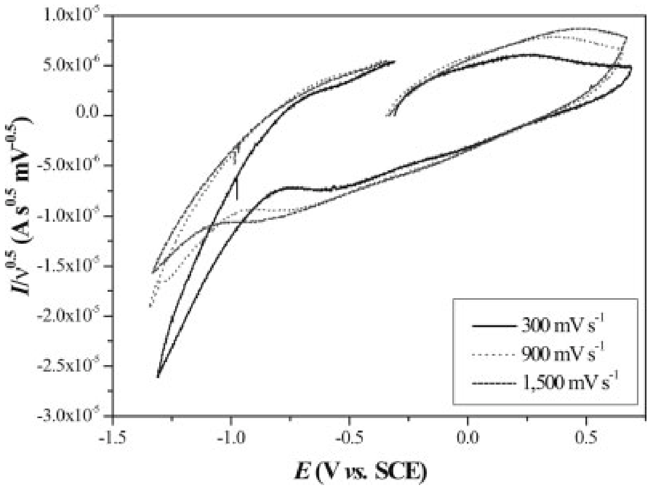

Figure 2. Normalized cyclic voltammograms for Ti-6Al-4V in a macrocell at 60°C. The nonoverlapping curves indicate that mass transport is not dominant in the kinetics of HAP electrodeposition.

of crystals with varying sizes. TEM also reveals that formation of nanosized cubical crystals is followed by growth of columnar single crystals with preferred orientation.[43,44] These experimental results support our claims for occurrence of both instantaneous and progressive nucleation mechanisms, as well as for transition from two-dimensional to three-dimensional growth. The evident porosity in Figure 4 is desirable with respect to biomedical applications, because it allows for ingrowth of tissues and enhanced fixation of implants. EDS semiquantitative analysis of the deposit shows that the calcium-to-phosphorus atomic ratio is within the range of 1.63–1.66, indicating the formation of the HAP phase. XRD spectra from the pure Ti-coated samples show that only the stoichiometric HAP phase is deposited on the substrate. The HAP exhibits a [002] preferred orientation, which correlates to the [002] preferred orientation of the pure Ti substrate surface. Analysis of XRD data leads to the conclusion that the content of the amorphous calcium phosphate phase in the electrodeposited coating is less than 5%, much lower than that in commercial plasma-sprayed coatings. Consequently, the solubility of the electrodeposited HAP in DI water during periods of as long as 240 h is very low, resulting in negligible release of calcium ions into solution and slower kinetics of bone apposition *in vivo*.[43,44]

Figure 5(a–d) present AFM deflection mode images that were taken *ex situ* after potentiostatic deposition on pure Ti at 85°C for varying periods. The deflection image, also known as the error signal image, represents the gradient of shape change and is thus more sensitive than topography images to delegate spatial information such as sharp edges. From Figure 5, it is evident that after 10 min the deposit structure is still two-dimensional, whereas after 30 min it is already three-dimensional. During the two-dimensional growth stage, the platelet crystals are smaller than 200 nm in length and width, and less than 20-nm thick (the latter dimension was determined by AFM line scans of the surface profile). As deposition proceeds, the platelets continue to grow in a preferred orientation [Fig. 5(c,d)], while accumulating within domains ~1 μm in diameter. The length and thickness of each platelet is of the order of 600 and 40 nm, respectively. These observations are in accordance with data from electrochemical measurements (Fig. 1), ESEM, and TEM.[43,44] The dimensions reported herein are less than one order of magnitude larger than those of biological apatites. This implies that the conditions *in vivo* limit the progressive nucleation stage and three-dimensional growth of apatite crystals, as will be discussed in the following section.

Preliminary experiments in a macrocell with a supporting electrolyte at 60°C show (Fig. 6) that a net current due to nucleation and growth of HAP may exist only at potentials that are more cathodic than −1.1 V versus SCE. Figure 7 presents a cyclic voltammogram [Fig. 7(a)] and a cathodic polarization curve [Fig. 7(b)] that were both constructed at a scan rate of 5 mV s^{-1}, as well as several AFM deflection images that were acquired *in situ* and in real time while constructing Figure 7(b). An arrow marks the forward scan in Figure 7(a). Note that the current density in the reverse scan is

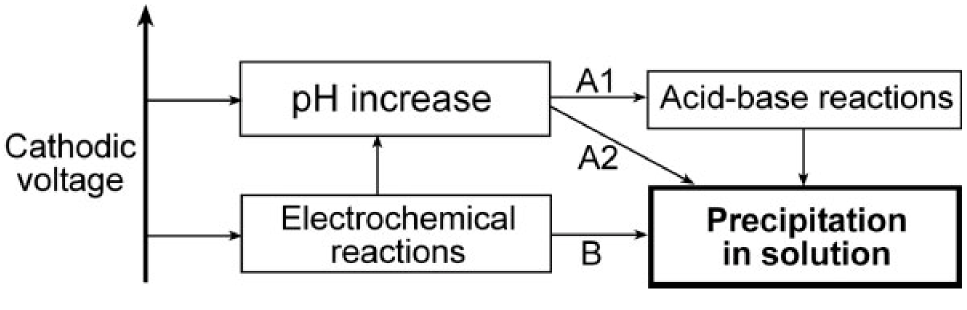

Figure 3. The processes that allow formation of HAP in electrolytes. Following route A1, the increase in pH first facilitates reactions (3.11) and (3.12). In route A2, the increase in pH lowers the solubility of the apatite phase in accordance with the solubility isotherms.[9] Following route B, the potential is cathodic enough to allow direct production of sufficient phosphate ions, according to reactions (3.8) and (3.9) (the former being more dominant).

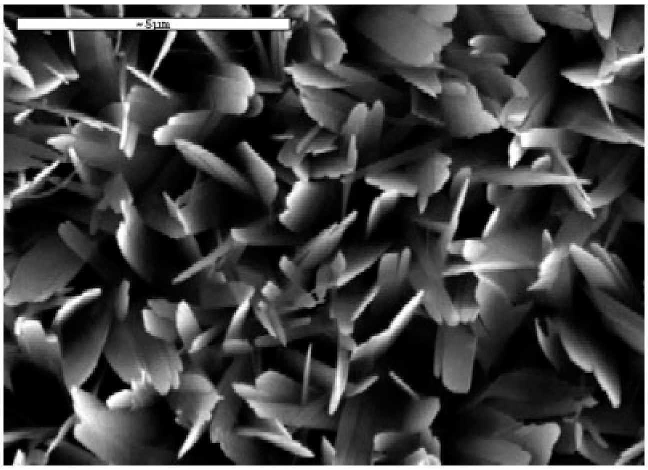

Figure 4. A SEM image demonstrating the platelet morphology and porosity on the surface of HAP electrodeposited in a macrocell on pure Ti at 85°C.

more negative than the current density in the forward scan. This behavior indicates that the deposition process is irreversible and that the kinetics of hydrogen evolution is faster on the surface of HAP in comparison to the surface of the titanium alloy. No horizontal plateau, indicative of the existence of a limiting current density, is noticed at the cathodic side of the voltammogram. This behavior has already been explained earlier. Furthermore, based on this cyclic voltammogram *per se*, the desirable potential range for electrodeposition of HAP may be −1.26 to −1.54 V versus SCE, before the hydrogen evolution reaction becomes dominant (as evident by a sharp, nearly linear, increase in the cathodic current density). The value −1.4 V versus SCE, at which potentiostatic deposition of HAP was carried out in the present work, falls within this range. The corresponding images (not included herein) showed that at a potential of −922 mV versus SCE no deposit had formed. At a potential of −1.23 V versus SCE, a noisy image due to hydrogen evolution in solution and only few deposit nucleation sites were observed. At a potential of −1.89 V versus SCE, the image was very noisy because of extensive hydrogen evolution, but a notable HAP deposit had already formed. Figure 7(c–f) present images that were acquired at four different potentials

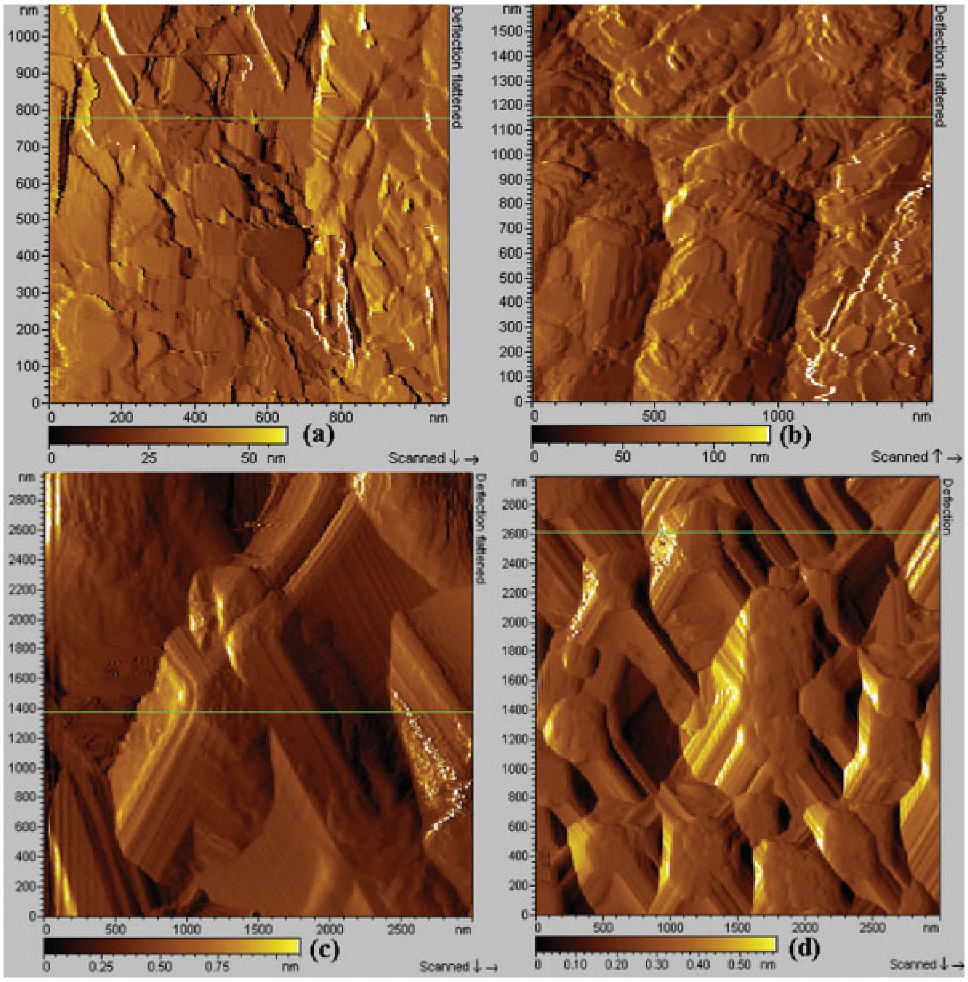

Figure 5. AFM deflection images acquired *ex situ* after 1 (a), 10 (b), 30 (c), and 60 (d) min deposition on pure Ti in a macrocell at 85°C. The transition from a two-dimensional growth to a three-dimensional growth is evident. [Color figure can be viewed in the online issue, which is available at www.interscience.wiley.com.]

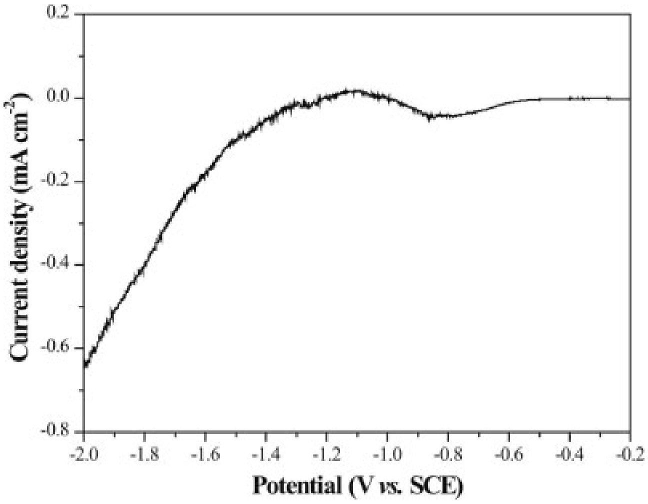

Figure 6. A subtracted cathodic polarization curve drawn in a macrocell at 60°C. This curve is the output of subtracting the cathodic polarization curve drawn in a supporting electrolyte from the curve drawn in the deposition electrolyte. It shows that electrodeposition is likely only at potentials more cathodic than −1.1 V versus SCE.

during cathodic polarization. Each potential value refers to the time at which an image scan (top to bottom) is completed. In Figure 7(d), two nuclei that did not reach a critical size and consequently dissolved [compare to Fig. 7(e)] are surrounded by circles. The construction of this image was completed at −842 mV versus SCE, which is not cathodic enough to overcome the free energy barrier for growth. For a process of nucleation of a hemispheric nucleus from an electrolyte, the classical Young-Dupré equation[45] may be reproduced as follows[32]:

$$\ln\frac{c_{\mathrm{sol}}}{c_{\mathrm{eq}}} = \frac{\Omega}{k_{\mathrm{B}}T}\frac{4(1-\cos\varphi)\gamma_{\mathrm{FL}} + 2\sin^2\varphi(\gamma_{\mathrm{SF}}-\gamma_{\mathrm{SL}})}{(2+\cos\varphi)(1-\cos\varphi)^2} \times \frac{1}{r_{\mathrm{cr}}} \tag{6}$$

where c_{sol} is the concentration of the deposit ions in the bulk of the electrolyte, c_{eq} is the solubility of the deposit material, Ω is the atomic volume of the deposit material, k_{B} is the Boltzmann constant, T is the absolute temperature, φ is the wetting angle, γ_{FL} is the deposit/electrolyte surface energy, γ_{SF} is the substrate/deposit surface energy, γ_{SL} is the substrate/electrolyte surface energy, and r_{cr} is the critical radius of the nucleus. Typical values of γ_{FL}, γ_{SF}, and γ_{SL} for HAP on titanium in electrolytes are around 35, 39, and 2.17 mJ m^{-2}, respectively. The values $c_{\mathrm{sol}} = 0.61$ m*M* and $T = 60°\mathrm{C}$ are chosen based on the experimental conditions in the present work. The mean atomic volume of the constituents of HAP is calculated from the periodic table as $\Omega = 3 \times 10^{-29}$ m^3 atom^{-1}. The values $\varphi = 6°$ and $r_{\mathrm{cr}} = 57$ nm are measured by a surface profile scan on a high-magnification AFM image of one of the unstable nuclei. Substituting these values into Eq. (6), c_{eq} is calculated to be 0.225 m*M*. The corresponding value for pH 6.5 is determined based on the solubility isotherm.[9] Substituting this value into Eq. (4) yields a calculated value $i = -247$ μA cm^{-2} as the critical current density for formation of HAP nuclei. The corresponding potential is −1.183 V versus SCE, according to the experimental cathodic polarization curve that was used in constructing Eq. (4). Returning to Figure 7(d), the potential was obviously not cathodic enough to provide the necessary electromotive for growth of stable nuclei. Therefore, both nuclei in this figure dissolved. Figure 7(e,f) were fully constructed at −1.21 and −1.57 V versus SCE, respectively. In these two images, HAP deposit is noticed between the topographically high β phase hills in the etched dual phase alloy. Interestingly, the HAP first nucleates on the α phase (hcp structure) and only later on the β phase (bcc structure). This behavior led to leveling of the coated surface as time elapsed. Hence, it may be concluded that the crystallographic misfit between the structure of the substrate and the coating plays an important role in electrodeposition of HAP.

In order to make sure that the real-time AFM images truly represent the nucleation and growth of HAP, one sample was analyzed in the SEM following EC-AFM study. Figure 8(a) shows a typical EDS spectrum from the coated surface. In addition to peaks of Ti, Al, and V from the substrate, peaks of Ca and P from the coating are clearly observed. A semiquantitative EDS analysis demonstrated a mean atomic ratio of 1.67 between the calcium and phosphorus atoms, indicating the formation of the stoichiometric HAP. Figure 8(b) shows a secondary electrons image that was taken as part of X-ray mapping. The corresponding element maps are shown in Figures 8c–e for Ti, Ca and P, respectively. By comparison to the secondary electrons image, it is evident that the bright charged area in Figure 8(b) is indeed a HAP deposit.

DISCUSSION AND CONCLUSIONS

This work presents the first direct, *in situ*, and real-time observation of the nucleation and growth of HAP by electrochemical reactions. The nucleation of HAP is influenced by the crystallographic structure and orientation of the metal substrate. In biological mineralization too, epitaxial considerations have been found to be of primary importance in understanding the formation of teeth and bones, as well as in pathological processes such as the development of urinary calculi.[30] Epitaxy, or oriented overgrowth, is a special case of heterogeneous nucleation in which the growth of the nuclei on the substrate follows a specific orientation. When the substrate and the deposit are made of different materials, the term heteroepitaxy is commonly used. Epitaxial behavior of two- and three-dimensional deposit phases exists if some or all of their lattice parameters coincide with those of the top

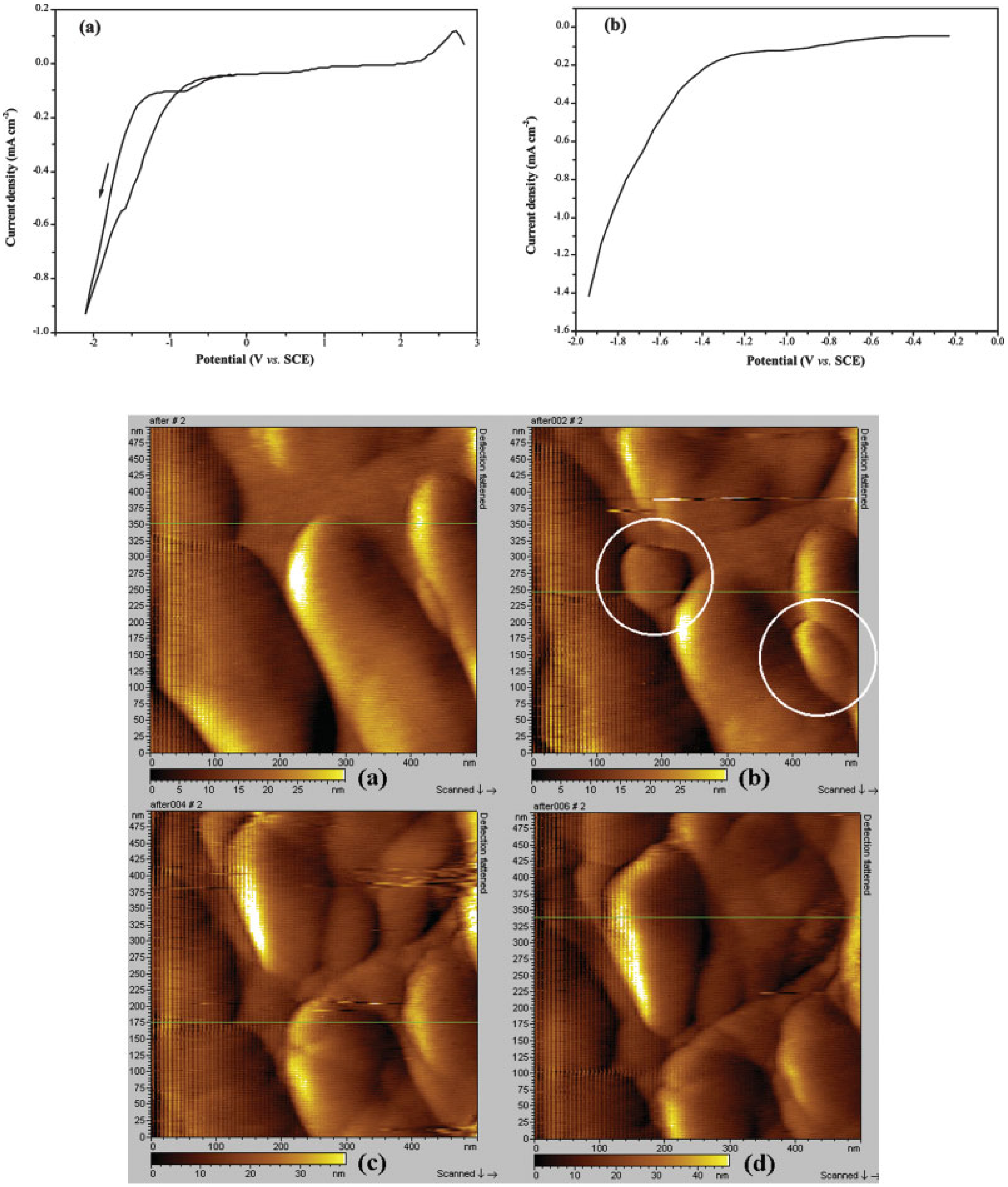

Figure 7. *In situ* and real-time EC-AFM under potentiodynamic conditions, demonstrating the potential dependence of the nucleation of HAP on Ti-6Al-4V at 60°C. (a) A typical cyclic voltammogram. (b) A cathodic polarization curve. (c–f) AFM deflection images acquired, while constructing (b), at −482 mV, −842 mV, −1.21 V, and −1.57 V versus SCE, respectively. [Color figure can be viewed in the online issue, which is available at www.interscience.wiley.com.]

layer of substrate. The epitaxy is determined by a minimum of the Gibbs function at constant temperature and pressure. Specifically organized organic surfaces have already been reported to induce growth of specifically oriented inorganic thin films either catalytically or epitaxially.[15] However, in the present study, no self-assembled organic templates or surfactants were used. Hence, this finding should affect both the material

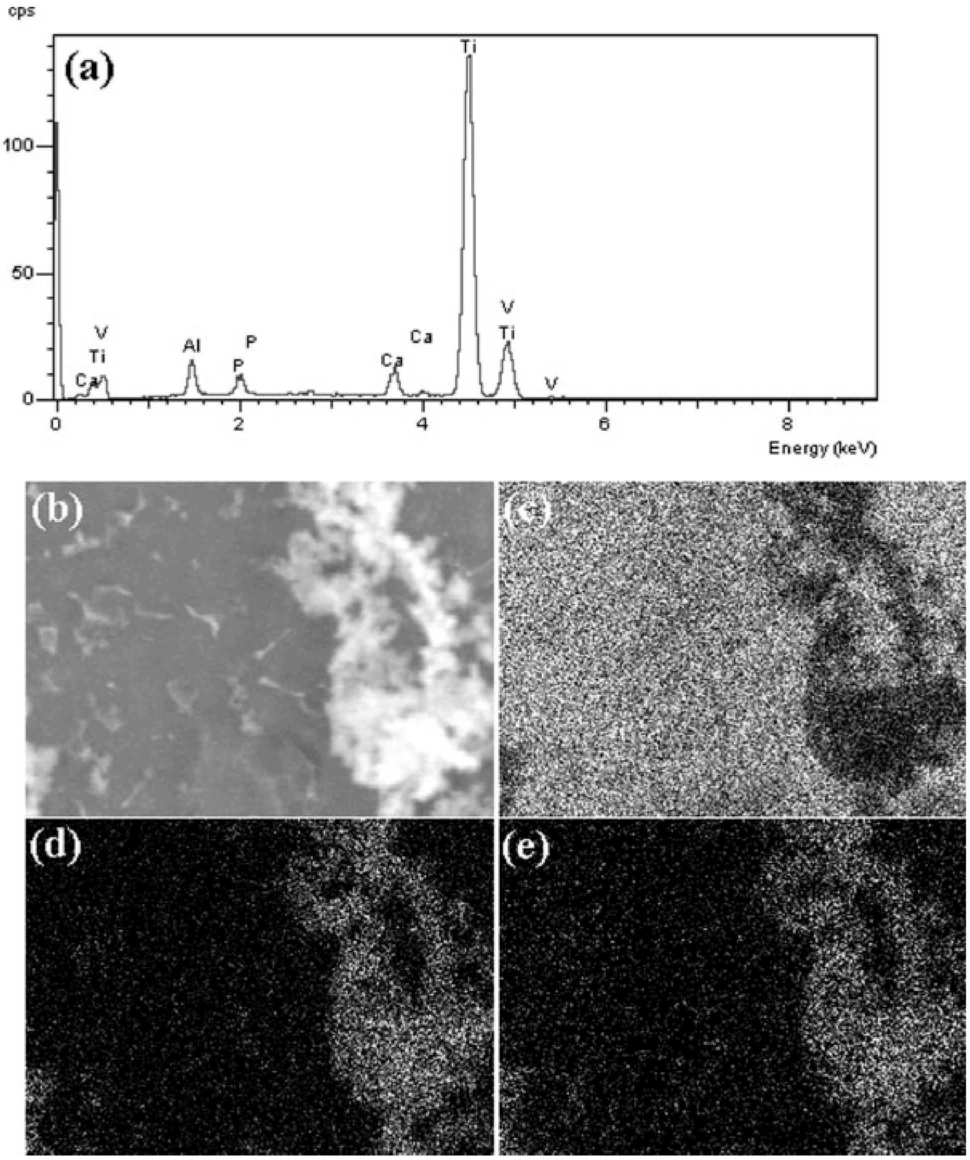

Figure 8. SEM analysis proving the formation of HAP during the EC-AFM study. (a) An EDS spectrum with Ca and P peaks. (b) A secondary electrons image with a bright-coated area. (c–e) X-ray maps of Ti, Ca, and P, respectively, which correspond to (b).

selection stage and the fabrication stage in future optimization of implants that are expected to integrate with bone. For example, materials for implants may be selected more carefully with respect to their heat treatment, which forms the preferable phases. Then, machining and forming should be carried out along specific crystallographic orientations.

The deposition of HAP is distinguished from typical electrodeposition processes by division into two stages. During the first 12 min or so, the nucleation is instantaneous and is accompanied by a two-dimensional growth. Subsequently, the nucleation becomes progressive and is accompanied by a three-dimensional growth. Interestingly, for bone mineralization in a given species, the average crystal size is smallest at formation and increases to maturity, at which time there is a leveling of this growth process.[4] The conditions in the human body apparently limit the growth of HAP *in vivo*. Indeed, several publications describe the effects that specific molecules have on the crystal growth of HAP. The most effective inhibitors seem to be polyanions, particularly polyphosphates or polyphosphonates. It was observed that salivary peptides and proteins, such as statherin and PRPs (praline-rich proteins), respectively, are powerful inhibitors. These macromolecules appear to prevent the precipitation of calcium phosphate phases in saliva in spite of the supersaturation of this secretion with respect to HAP. The inhibiting mechanism was related to their adsorption onto the surface of apatite seeds.[41] Proteoglycans, even at low concentrations, can delay or prevent apatite formation. On the other hand, bone collagen is considered to be intimately involved in the nucleation of bone mineral.[4]

Charge transfer is more dominant than mass transport in controlling the kinetics of deposition. This finding is somehow in contradiction to previous reports that focused on mass transport in nucleation and growth of HAP. However, in most cases, this was an assumption rather than based on electrochemical and other direct measurements. The pH that raises during deposition makes the formation of HAP more favorable thermodynamically, compared to other calcium phosphate phases, although it does not become high enough to make chemical reactions significant in production of phosphate ions. The direct decomposition of dihydrogen phosphate ions is more significant than decomposition of hydrogen phosphate ions in production of the phosphate ions, which are necessary for the precipitation of HAP. Physical precipitation of HAP in the electrolyte is possible because the concentration of calcium ions is much higher than the concentration of hydrogen ions. Applying a potential within the range of -1.26 to -1.54 V versus SCE is mandatory in order to form useful HAP by electrochemical processing in the specific electrolyte. This direct observation demonstrates the power of using EC-AFM when studying the effects of substrate surface, bath chemistry, and process parameters on the structure and related properties of HAP.

It is anticipated that EC-AFM becomes more common in the optimization of electrochemical processing for biomedical applications in the coming years. In addition, the body environment is very complex from an electrochemical point of view. All mineralization processes involve the precipitation of inorganic phases from solution. It has already been argued that homogeneous nucleation of particles in the solution will only dominate at relatively high levels of supersaturation where the precipitation process becomes kinetically controlled.[15] On the other hand, formation of the inorganic phase directly on a substrate (i.e., heterogeneous nucleation) is the dominant precipitation mechanism in the case of thermodynamically controlled systems. The synthesis of inorganic crystalline or amorphous minerals, such as HAP, fluoroapatite, calcium carbonate, and magnetite by living organisms, is therefore highly dependent on the local conditions such as ion concentrations, pH, and potential. The EC-AFM may aid in better understanding the biomineralization and other biomimetic processes on metals or other solid surfaces (e.g., organic scaffolds). A first trial in this direction has started in our lab, simulating the interstitial fluid environment at 37°C.

The authors thank E. Gileadi and T.M. Sridhar for discussions and comments, D. Ashkenazi and M. Levinshtein for technical assistance, and O. Nissan for electrical discharge machining.

References

1. Hong SB, Eliaz N, Leisk GG, Sachs EM, Latanision RM, Allen SM. A new Ti-5Ag alloy for customized prostheses by three-dimensional printing (3DP^{TM}). J Dent Res 2001;80:860–863.
2. Guiu J. Synthesis of Hydroxyapatite with Adsorbed and Intercrystalline Biomolecules. Cambridge, MA: MIT; 1999.
3. de Leeuw NH. Local ordering of hydroxy groups in hydroxyapatite. Chem Commun 2001;17:1646, 1647.
4. Betts F, Blumenthal NC, Posner AS. Bone mineralization. J Cryst Growth 1981;53:63–73.
5. Benezra V, Spector M, Hobbs LW. Characterization of mineral deposits on plasma-sprayed HA-coated Ti-6Al-4V. In: Cotell CM, Meyer AE, Gorbatkin SM, Grobe GL, editors. Proceedings of the 1995 Materials Research Society Fall Meeting. Pittsburgh, PA: MRS; 1996. Vol. 414, pp 165–170.
6. Danilchenko SN, Kukharenko OG, Moseke C, Protsenko IY, Sukhodub LF, Sulkio-Cleff B. Determination of the bone mineral crystallite size and lattice strain from diffraction line broadening. Cryst Res Technol 2002;37:1234–1240.
7. Nyman JS, Reyes M, Wang X. Effect of ultrastructural changes on the toughness of bone. Micron 2005;36:566–582.
8. Paunovic M, Schlesinger M. Fundamentals of Electrochemical Deposition. New York: Wiley; 1998.
9. Brown WE, Chow LC. Chemical properties of bone mineral. Annu Rev Mater Sci 1976;6:213–236.
10. Fernández E, Gil FJ, Ginebra MP, Driessens FCM, Planell JA, Best SM. Calcium phosphate bone cements for clinical applications. I. Solution chemistry. J Mater Sci: Mater Med 1999;10: 169–176.
11. Vijayaraghavan TV, Bensalem A. Electrodeposition of apatite coating on pure titanium and titanium alloys. J Mater Sci Lett 1994;13:1782–1785.
12. Eliaz N, Sridhar TM, Rosenberg Yu. Electrodeposition of hydroxyapatite on titanium for implants. In: Lütjering G, Albrecht J, editors. Proceedings of the 10th World Conference on Titanium. Weinheim, Germany: Wiley-VCH; 2004. Vol. 5, pp 3299–3306.
13. Manso M, Jimenez C, Morant C, Herrero P, Martinez-Duart JM. Apatite films produced by electrodeposition: Characterization by TEM and AFM. Surf Interface Anal 2001;31:1104–1109.
14. Huaxia J, Ponton CB, Marquis PM. Microstructural characterization of hydroxyapatite coating on titanium. J Mater Sci: Mater Med 1992;3:283–287.
15. Aksay IA, Trau M, Manne S, Honma I, Yao N, Zhou L, Fenter P, Eisenberger PM, Gruner SM. Biomimetic pathways for assembling inorganic thin films. Science 1996;273:892–898.
16. Onuma K, Ito A, Tateishi T, Kameyama T. Surface observations of synthetic hydroxyapatite single crystal by atomic force microscopy. J Cryst Growth 1995;148:201–206.
17. Budevski E, Staikov G, Lorenz WJ. Electrochemical Phase Formation and Growth: An Introduction to the Initial Stages of Metal Deposition. Weinheim, Germany: VCH; 1996. pp 4–6, 163–165, 184, 185, 280–283, 342.
18. Fleischmann M, Thirsk HR. Metal deposition and electrocrystallization. In: Delahay P, editor. Advances in Electrochemistry and Electrochemical Engineering, Vol. 3. New York: Wiley; 1963. p 123.
19. Milchev A. Electrochemical alloy formation—Theory of progressive and instantaneous nucleation without overlap. Electrochim Acta 1997;42:1533–1536.
20. Abyaneh MY. Extracting nucleation rates from current–time transients. I. The choice of growth models. J Electroanal Chem 2002;530:82–88.
21. Frank FC, van der Merwe JH. One-dimensional dislocations. I. Static theory. Proc R Soc London Ser A 1949;198:205–216.
22. Volmer M, Weber A. Germ formation in oversaturated figures. Z Physik Chem 1926;119:277–301.

23. Stranski IN, Krastanov L. Zur theorie der orientierten ausscheidung von ionenkristallen aufeinander. Sitzungsber Akad Wiss Wien Math 1938;146:797–801.
24. Scharifker B, Hills G. Theoretical and experimental studies of multiple nucleation. Electrochim Acta 1983;28:879–889.
25. Scharifker BR, Mostany J, Palomar-Pardavé M, González I. On the theory of the potentiostatic current transient for diffusion-controlled three-dimensional electrocrystallization processes. J Electrochem Soc 1999;146:1005–1012.
26. Oskam G, Long JG, Natarajan A, Searson PC. Electrochemical deposition of metals onto silicon. J Phys D: Appl Phys 1998;31:1927–1949.
27. D'Ajello PCT, Munford ML, Pasa AA. Transient equations for multiple nucleation on solid electrodes: A stochastic description. J Chem Phys 1999;111:4267–4272.
28. Barin CS, Correia AN, Machado SAS, Avaca LA. The effect of concentration on the electrocrystallization mechanism for copper on platinum ultramicroelectrodes. J Braz Chem Soc 2000; 11:175–181.
29. Mafé S, Manzanares A, Reiss H, Thomann JM, Gramain P. Model for the dissolution of calcium hydroxyapatite powder. J Phys Chem 1992;96:861–866.
30. Koutsoukos PG, Nancollas GH. Crystal growth of calcium phosphates—Epitaxial considerations. J Cryst Growth 1981;53: 10–19.
31. Zhang JM, Lin CJ, Feng ZD, Tian ZW. Mechanistic studies of electrodeposition of bioceramic coatings of calcium phosphates by an in situ pH-microsensor technique. J Electroanal Chem 1998;452:235–240.
32. Eliyahu M. Master's dissertation. The Use of Electrochemical Scanning Probe Microscopy to Study In Situ the Processes of Nucleation and Growth as Well as the Microstructure of Hydroxyapatite Electrodeposited on a Titanium Alloy for Biomedical Applications. Tel-Aviv, Israel: Tel-Aviv University; 2005.
33. Bruins HR. Coefficients of diffusion in liquids. In: Washburn EW, editor. International Critical Tables of Numerical Data, Physics, Chemistry and Technology, Vol. 5. New York: McGraw-Hill; 1929. p 63.
34. Bard AJ, Faulkner LR. Electrochemical Methods: Fundamental and Applications. New York: Wiley; 2001.
35. Huang LY, Xu KW, Lu J. A study of the process and kinetics of electrochemical deposition and hydrothermal synthesis of hydroxyapatite coatings. J Mater Sci: Mater Med 2000;11:667–673.
36. Kumar M, Dasarathy H, Riley C. Electrodeposition of brushite coatings and their transformation to hydroxyapatite in aqueous solutions. J Biomed Mater Res 1999;45:302–310.
37. Kuo MC, Yen SK. The process of electrochemical deposited hydroxyapatite coatings on biomedical titanium at room temperature. Mater Sci Eng C 2002;20:153–160.
38. Redepenning J, Schlessinger T, Burnham S, Lippiello L, Miyano J. Characterization of electrolytically prepared brushite and hydroxyapatite coatings on orthopedic alloys. J Biomed Mater Res 1996;30:287–294.
39. Shirkhanzadeh M. Direct formation of nanophase hydroxyapatite on cathodically polarized electrodes. J Mater Sci: Mater Med 1998;9:67–72.
40. Yen SK, Lin CM. Cathodic reactions of electrolytic hydroxyapatite coating on pure titanium. Mater Chem Phys 2002;77:70–76.
41. Moreno EC, Varughese K. Crystal growth of calcium apatites from dilute solutions. J Cryst Growth 1981;53:20–30.
42. Brown WE, Chow LC. Thermodynamics of apatite crystal growth and dissolution. J Cryst Growth 1981;53:31–41.
43. Wang H. Investigation of Bone Response to Implant Materials by Electron Microscopy and Computer Simulation. Cambridge, MA: MIT; 2004.
44. Wang H, Eliaz N, Xiang Z, Hsu HP, Spector M, Hobbs LW. Early bone apposition in vivo on plasma-sprayed and electrochemically deposited hydroxyapatite coatings on titanium alloy. Biomaterials 2006;27:4192–4203.
45. Howe JM. Bonding, structure and properties of metal/ceramic interfaces. I. Chemical bonding, chemical reaction, and interfacial structure. Int Mater Rev 1993;38:233–256.